

# The Kelvin-Helmholtz/von Neumann Stability of Discrete Representations of the Two-Fluid Model for Stratified Two-Phase Flow

A.H. AKSELSEN

Norwegian University of Science and Technology,  
Department of Energy and Process Engineering, Kolbjørn Hejes v. 1B, 7491 Trondheim, Norway.  
[andreas.h.akselsen@ntnu.no](mailto:andreas.h.akselsen@ntnu.no)

## Abstract

Many dynamic pipe flow simulator tools are capable of predicting the onset of hydrodynamic flow instability through detailed simulation. These instabilities provide a natural mechanism for flow regime transition. The quality and reliability of flow predictions are however strongly dependent upon the numerics within these simulator tools, the scheme type and resolution in particular.

A Kelvin-Helmholtz stability analysis for the differential two-fluid model is in the present work presented and extended to discrete representations of said model. This analysis provides algebraic expressions which give instantaneous, quantitative information into i) when a studied scheme will predict linear wave growth, ii) the rate of growth and the expected growing wavelength, and iii) the wave speeds. These stability expressions adhere to a wider family of finite volume methods, directly applicable to any specific formulation within this group. Both the spatial and temporal discretization are found to play decisive roles in a method's predictive capability. Fundamental aspects of how numerical errors from the temporal integration affects the predicted stability are explored. Numerical errors are observed to manifest in increased, as well as reduced, wave growth. Low-frequency growth from numerical errors is not always easily distinguished from physical wave growth. The linear analysis is demonstrated to be useful in understanding the predictions made by simulator tools, and in choosing the appropriate numerical method and simulation parameters for optimizing the simulation efficiency and reliability.

## 1 Introduction

Stability analyses of the two-fluid model have been performed by numerous authors. For example, Taitel and Dukler [Taitel and Dukler 1976/01/] used linear theory with a simplified, inviscid two-fluid model to predict flow regime transition to slug flow. Barnea and Taitel [Barnea and Taitel 1993] presented a derivation of the Kelvin-Helmholtz stability criterion for viscous flows (henceforth abbreviated the

VKH criterion) and examined the non-linear flow development through simulation [Barnea and Taitel 1994]. Barnea also performed a stability analysis on a discrete upwind type scheme of a simplified version of the two-fluid model for annular flow [Barnea 1991/11/]. Here it was shown again how an intrinsically unstable, ill-posed differential model may display stable behaviour if provided with sufficient numerical diffusion. (The annular interface is inherently unstable locally though it may be stable in a statistical sense.) Barnea argued that the discrete model can be regarded as a legitimate model for the average flow, even though the differential model is ill-posed.

Issa and Kempf [Issa and Kempf 2003] have been credited with first demonstrating that the predicted wave growth from transient simulations of the full two-fluid model coincides with the wave growth from Kelvin-Helmholtz theory, and suggested that such simulated wave growth gives a natural transition into a wavy or slugging flow regime.

In [Stewart 1979], Stewart presented a von Neumann analysis on two variants of the two-fluid model, one with a term exchanging momentum between the phases and one without. The two-fluid model is known for obtaining complex eigenvalues if the momentum exchange is insufficient, which means that the model can no longer be deemed part of a well-posed hyperbolic initial value problem [Gidaspow 1995]. Stewart showed that *well-behaved* discrete solutions, *i.e.*, steady flow solutions, were obtainable on discretizations of non-hyperbolic systems, provided the mesh resolution was restricted.

Liao et al. [Liao et al. 2008] performed a linear stability study on a discrete two-fluid model with a staggered grid arrangement, comparing various interpolations for the convection term. This analysis was limited to implicit time integration, considering the convection terms only. Numerical errors arising from the dislocation of staggered information, as well as from the conservative formulation, appears to have been neglected. The paper concluded that the central difference discretization was superior to the first and higher order non-centred interpolations. Liao et al. also examined the evolution of the wavelength distributions from a random initial disturbance, and the behaviour as the model turns ill-

posed.

The light water reactor safety analysis codes RELAP5 and CATHARE have also been studied with von Neumann analysis by Pokharna et al.. Pokharna et al. [1997], looking into how numerical diffusion and terms added to achieve model hyperbolicity affect stability predictions. They found the numerical regularization to be dominant in the cases studied. Fullmer et al. Fullmer et al. [2014] performed similar analyses on an upwind discretization of the two-fluid model, demonstrating the mesh size dependency of the predicted stability in both the linear and nonlinear range. A Reynolds stress modelling was shown provide grid independent regularization.

The present article focuses on providing general theory for a wider family of discrete two-fluid model representations. This will be done by relating the predicted growth and decay of the discrete representations directly to the growth results of the Kelvin-Helmholtz analysis of the differential two-fluid model. Linear theory of the type here presented is demonstrated to be powerful tool when it comes to assessing the predictive capability of any chosen discrete representation, providing support with decisions related to the parametric setup prior to simulation and interpreting the simulation results. *Predictive capability* here refers to the reliability and accuracy with which a discrete representation predicts wave growth or decay under limited computational resolution. It will be shown that the growth and dispersion response of discrete representations is perfectly analogous to that of the differential model. What's more, the differential Kelvin-Helmholtz expression directly provides that growth and dispersion which will be predicted by the discrete methods in the linear range, provided these representations uses the same discrete differentiations all over.

## 2 The Two-Fluid Model

The compressible, adiabatic, equal pressure four-equation two-fluid model for stratified pipe flow results from an averaging of the conservation equations across the cross-section area. The model is commonly written

$$\partial_t(\rho a)_\kappa + \partial_x(\rho a u)_\kappa = 0, \quad (2.1a)$$

$$\partial_t(\rho a u)_\kappa + \partial_x(\rho a u^2)_\kappa + a_\kappa \partial_x p_i + \rho_\kappa a_\kappa g \cos \theta \partial_x h = s_\kappa, \quad (2.1b)$$

$$a_\ell + a_g = \mathcal{A}, \quad (2.1c)$$

$$p_i = \mathcal{P}_g(\rho_g) = \mathcal{P}_\ell(\rho_\ell). \quad (2.1d)$$

Field  $\kappa$ , occupied by either gas,  $\kappa = g$ , or liquid,  $\kappa = \ell$ , is segregated from the other field. Subscript i indicates the fluid interface; see Figure 2.1.  $p_i$  is here the pressure at the interface, assumed the same for each phase and given by some equation of state  $\mathcal{P}$ .  $h$  is the height of the interface from the pipe floor, and the term in which it appears originates from approximating a hydrostatic wall-normal pressure distribution.  $u_\kappa$  and  $\rho_\kappa$  are the mean

fluid velocity and density in field  $\kappa$ . The momentum sources are  $s_\kappa = -\tau_\kappa \sigma_\kappa \pm \tau_i \sigma_i - a_\kappa \rho_\kappa g \sin \theta$ , where  $\tau$  is the skin frictions at the walls and interface.  $\theta$  is the pipe inclination, positive above datum, and  $g$  is the gravitational acceleration.

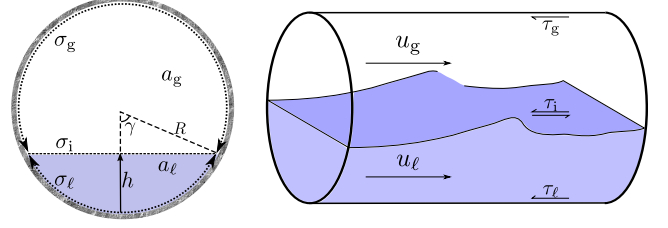


Figure 2.1: Pipe cross-section

The circular pipe geometry itself enters into the modelling through the relation between the level height  $h$ , the specific areas  $a_\kappa$  and the peripheral lengths  $\sigma_\kappa$  and  $\sigma_i$ . These are algebraically interchangeable through a geometric function

$$h = \mathcal{H}(a_\ell) \quad (2.2)$$

whose derivative is  $\mathcal{H}' = 1/\sigma_i$ . See e.g. Akselsen [2016a] for expressions of the geometric relationships.

Fluid compressibility is commonly ignored when considering the surface wave stability of (2.1). This enables us to base the stability analysis on the incompressible two-fluid model, which has lower rank and a conservative form.

Assuming incompressible phases, the two-equation model is obtained by reducing the momentum equations with their respective mass equations and eliminating the pressure term between them, resulting in

$$\partial_t \mathbf{v} + \partial_x \mathbf{f} = \nu \partial_{xx} \mathbf{v} + \mathbf{s} \quad (2.3)$$

with conserved variables and fluxes

$$\mathbf{v} = (a_\ell, \rho_\ell u_\ell - \rho_g u_g)^T, \quad \mathbf{f} = (q_\ell, j)^T, \quad \mathbf{s} = (0, s)^T.$$

Symbols for the flux and source components have here been defined and are

$$\begin{aligned} q_\kappa &= a_\kappa u_\kappa, & j &= \frac{1}{2}(\rho_\ell u_\ell^2 - \rho_g u_g^2) + m_y h, \\ s &= -m_x - \frac{\tau_\ell \sigma_\ell}{a_\ell} + \frac{\tau_g \sigma_g}{a_g} + \tau_i \sigma_i \left( \frac{1}{a_\ell} + \frac{1}{a_g} \right), \\ \nu &= 0. \end{aligned}$$

A dummy viscous term has been added to the system, the purpose of which lies in evaluating the artificial numerical viscosity present in some discrete representations. Specific weight coefficients have been grouped into  $m_x = (\rho_\ell - \rho_g)g \sin \theta$  and  $m_y = (\rho_\ell - \rho_g)g \cos \theta$ . The identities

$$a_\ell + a_g = \mathcal{A}(x), \quad q_\ell + q_g = \mathcal{Q}(t), \quad (2.4)$$

where the latter has been obtained from summing the two mass equations, close the model. Both  $\mathcal{A}$  and  $\mathcal{Q}$  are

parametric.

Finally, the eigenstructure of (2.3) is useful to know. The Jacobian of  $\mathbf{f}$  is

$$\frac{\partial \mathbf{f}}{\partial \mathbf{v}} = \frac{1}{\rho^*} \begin{pmatrix} (\rho u)^* & 1 \\ \varkappa^2 & (\rho u)^* \end{pmatrix}, \quad (2.5)$$

whose eigenvalues are

$$\lambda^\pm = \frac{(\rho u)^* \pm \varkappa}{\rho^*}. \quad (2.6)$$

A new variable

$$\varkappa = \sqrt{\rho^* m_y \mathcal{H}' - \frac{\rho \ell \rho_g}{a_\ell a_g} (u_g - u_\ell)^2}. \quad (2.7)$$

has here been introduced along with the operator

$$\psi^* = \frac{\psi_\ell}{a_\ell} + \frac{\psi_g}{a_g}. \quad (2.8)$$

### 3 Kelvin-Helmholtz Stability

The viscous Kelvin-Helmholtz (VKH) stability analysis is here presented in some detail, which will later be related directly to the stability of discrete representations.

*Variable of the steady state  $\mathbf{v} = \mathbf{V}$  will in the following be assigned upper-case symbols.*<sup>1</sup> The steady state solution  $\mathbf{V}$  satisfies the so-called *holdup equation*

$$s(\mathbf{V}) = S = 0. \quad (3.1)$$

linearizing (2.3) about the steady state,

$$\mathbf{v} = \mathbf{V} + \tilde{\mathbf{v}},$$

yields

$$\left( \mathbb{I}(\partial_t - \nu \partial_{xx}) + \frac{\partial \mathbf{F}}{\partial \mathbf{V}} \partial_x - \frac{\partial \mathbf{S}}{\partial \mathbf{V}} \right) \tilde{\mathbf{v}} = \mathbf{0}. \quad (3.2)$$

Let's briefly look at the general solution of (3.2). It may be written

$$\tilde{\mathbf{v}}(x, t) = \sum_k \mathbb{P}^{-1} e^{ik(x - C_k t)} \mathbb{P} \hat{\mathbf{v}}_k^0 \quad (3.3)$$

where  $e^{-ikC_k t} = \text{diag}_p(e^{-ikc_{k,p} t})$ ,  $c_{k,p}$  being the  $p$ -th eigenvalues of  $\mathbb{H}_k = \frac{\partial \mathbf{F}}{\partial \mathbf{V}} - ik\nu \mathbb{I} + \frac{i}{k} \frac{\partial \mathbf{S}}{\partial \mathbf{V}}$  and  $\mathbb{P}$  containing their corresponding eigenvectors.  $\hat{\mathbf{v}}_k^0$  are the Fourier modes of the initial conditions.

*Proof.* Solution (3.3) satisfies the initial conditions by virtue of  $\hat{\mathbf{v}}_k^0$  being the Fourier modes of these and  $e^{-ikC_k \cdot 0} = \mathbb{I}$ . Further we have

$$\begin{aligned} \partial_t \mathbb{P}^{-1} e^{-ikC t} \mathbb{P} &= \mathbb{P}^{-1} \text{diag}_p(-ikc_p e^{-ikc_p t}) \mathbb{P} \\ &= \mathbb{P}^{-1} (-ikC) e^{-ikC t} \mathbb{P} = -ik \mathbb{H} \mathbb{P}^{-1} e^{-ikC t} \mathbb{P}. \end{aligned}$$

<sup>1</sup>The state  $\mathbf{V}$  could also be non-uniform provided the perturbation wavelengths are much smaller than the length scales of the flow state Pokharna et al. [1997].

Directly inserting (3.3) into (3.2) then yields

$$\sum_k \left( -ik \mathbb{H}_k + k^2 \nu \mathbb{I} + \frac{\partial \mathbf{F}}{\partial \mathbf{V}} ik - \frac{\partial \mathbf{S}}{\partial \mathbf{V}} \right) \mathbb{P}^{-1} e^{ik(x - C_k t)} \mathbb{P} \hat{\mathbf{v}}_k = \mathbf{0}.$$

The bracket term cancels at each wavenumber due to the definition of  $\mathbb{H}_k$ .  $\square$

So, the linear response of the system will be through the growth and dispersion of a number of linear waves. We will not bother too much with this general solution, but are interested in the stability behaviour of (3.2) – stable flow occurs if the real component of all eigenvalues is negative or zero. The solution (3.3) is just a linear combination of waves; we re-write it to the form

$$\tilde{\mathbf{v}}(x, t) = \sum_k \sum_{p=1,2} \hat{\mathbf{v}}_{k,p} e^{ik(x - c_{k,p} t)}. \quad (3.4)$$

Inserting (3.4) into (3.2) yields the algebraic system

$$\sum_k \sum_{p=1,2} \frac{\partial \mathbf{E}_{k,p}}{\partial \mathbf{V}} \hat{\mathbf{v}}_{k,p} e^{ik(x - c_{k,p} t)} = \mathbf{0}, \quad (3.5)$$

with

$$\mathbf{E}_{k,p} = \mathbf{V}(\delta_t^{k,p} - \nu \delta_{xx}^k) + \mathbf{F} \delta_x^k - \mathbf{S}. \quad (3.6)$$

Each  $p$ -term must solve (3.5) individually if the sum is to be a solution at all times. Suppressing both sum indices we simply write

$$\frac{\partial \mathbf{E}}{\partial \mathbf{V}} \hat{\mathbf{v}} = \mathbf{0}. \quad (3.7)$$

The  $\delta$ -operators appearing in (3.6), accounting for the effect of the partial derivatives, are defined

$$\delta \equiv \frac{\partial \exp ik(x - ct)}{\exp ik(x - ct)}. \quad (3.8)$$

Note that these are simple scalars effectively flipping the various terms straight angles in the complex plane:

$$\delta_t = -ikc, \quad \delta_x = ik, \quad \delta_{xx} = -k^2.$$

Using  $\delta$  operators will allow solutions to be extended directly to discrete representations.

Because (3.7) is linear we may express it uniquely in terms of one of the disturbance properties, say  $\hat{a}_\ell : \frac{\partial \mathbf{V}}{\partial A_\ell} \hat{a}_\ell = \hat{\mathbf{v}}$ , yielding

$$\mathbf{E}' = \mathbf{0}, \quad (3.9)$$

where  $\Psi' \equiv \frac{d\Psi}{dA_\ell}$ . We further define a viscous phase celerity

$$c_\nu \equiv -\frac{\delta_t - \nu \delta_{xx}}{\delta_x}, \quad (3.10)$$

which evaluates to  $c_\nu = c + ik\nu$ . Inserting (3.6) and (3.10) into (3.9) now yields

$$\mathbf{F}'_\nu \delta_x - \mathbf{S}' = \mathbf{0}. \quad (3.11)$$

The components of  $\mathbf{F}_r$  are the fluxes in a relative frame, moving with (complex) velocity  $c_\nu$ .  $\mathbf{F}_r$  equals  $\mathbf{F}$  with the relative velocities

$$U_{\kappa,r} = U_\kappa - c_\nu$$

replacing  $U_\kappa$ . Since the mass equation contains no source term, the first component of (3.11), combined with (2.4), yields directly

$$Q_{\kappa,r} = A_\kappa U_{\kappa,r} = \text{const.}, \quad (3.12)$$

which relates both velocity components to  $A_\ell$ . The second component of (3.11) yields the *dispersion equation*

$$J'_r \delta_x - S' = 0, \quad (3.13)$$

where  $\delta_x = ik$ . Using (3.12) one finds

$$J'_r \equiv \frac{dJ_r}{dA_\ell} = m_y \mathcal{H}' - (\rho U_r^2)^* \quad (3.14)$$

(see (2.8)) and

$$S' \equiv \frac{dS}{dA_\ell} = S_{A_\ell} + c_\nu (S_{Q_\ell} - S_{Q_g}). \quad (3.15)$$

The source has here been parameterised as function of  $A_\ell$  and  $Q_\kappa$  with

$$S_{A_\ell} = \left( \frac{\partial \mathcal{S}}{\partial A_\ell} \right)_{Q_\ell, Q_g}, \quad S_{Q_\ell} = \left( \frac{\partial \mathcal{S}}{\partial Q_\ell} \right)_{A_\ell, Q_g}, \quad S_{Q_g} = \left( \frac{\partial \mathcal{S}}{\partial Q_g} \right)_{A_\ell, Q_\ell}$$

easily computed for any source  $\mathcal{S}$  from discrete state differentials.

Some alternative forms of presenting  $J'_r$  should also be pointed out, namely

$$J'_r = \frac{\varkappa^2 - ((\rho U_r)^*)^2}{\rho^*} = -\rho^* \det \left( \frac{\partial \mathbf{F}_r}{\partial \mathbf{V}} \right) = -\rho^* \lambda_r^+ \lambda_r^-. \quad (3.16)$$

Extracting any particular growth rate or wave celerity from (3.13) is perfectly straight forward and yields

$$c_\nu = b_1 \pm \sqrt{b_1^2 - b_0} \quad (3.17)$$

with

$$b_1 = \frac{1}{\rho^*} \left( (\rho U)^* - \frac{1}{2} \frac{S_{Q_\ell} - S_{Q_g}}{\delta_x} \right), \quad b_0 = \frac{1}{\rho^*} \left( \frac{S_{A_\ell}}{\delta_x} - J' \right),$$

and the definitions (3.10), (3.8) and (3.4). The wave resulting from plus in (3.17) will in the following be termed the ‘fast wave’. Conversely, the minus wave will be termed the ‘slow wave’.

In the case where  $\nu = 0$ , the marginal stability condition  $c_k \in \mathbb{R}$ , often called the VKH criterion, has a particularly simple solution. Both  $J'_r$  and  $S'$  are real in this case, so that (3.13) boils down to

$$S' = 0, \quad J'_r = 0, \quad (3.18)$$

with  $S = 0$  from the holdup equation (3.1). We may therefore regard the VKH criterion as the equilibrium state with respect to changes in phase fraction in the frame of a moving wave perturbation.  $S' = 0$  then gives the critical wave celerity  $c_{\text{crit}}$  and wave growth will occur if  $J'_r(c_{\text{crit}}) < 0$ .

Note that the rate of growth will in (3.13) depend upon the wavenumber  $k$  (present in  $\delta_x$ ) but that the condition for marginal stability, (3.18), will not.

These results are identical to those provided in e.g., Barnea and Taitel [1993], Holmås [2010], Liao et al. [2008], though a different approach has been chosen which provides a physical interpretation.

## IKH

Let us conclude this section by remarking on some features of the so-called *inviscid Kelvin-Helmholtz* stability criterion (IKH.) This is the stability of the two-fluid model (2.3) without the source term;  $s \equiv 0$ . From (3.16) we do however see that celerity  $c$  must turn complex if the eigenvalues do. The IKH criterion is thus really a test on hyperbolicity. Inspecting the eigenvalues (2.6), the ‘inviscid Kelvin-Helmholtz’ (IKH) criterion can thus be written

$$\text{IKH neutral stability:} \quad \varkappa = 0.$$

From (3.16) we then find the ‘inviscid’ critical celerity

$$c_{\text{iv,crit}} = \lambda_{\text{iv,crit}}^+ = \lambda_{\text{iv,crit}}^- = (\rho u)^* / \rho^*.$$

Notice that the condition for IKH marginal stability,  $\varkappa = 0$ , does *not* coincide with the VKH criterion (3.18) in the inviscid limit  $S \rightarrow 0$ . This feature is illustrated in Figure 3.1, showing  $c$  in the complex plane with the parameters and closures described later in Section 5.2. For clarity, only the superficial gas velocity  $Q_g/A$  is altered and the source  $S$  is reduced sequentially towards zero by multiplying it by constant weights. This does not change the critical state, as long as  $S \neq 0$ , but the rate of growth near the point of marginal VKH stability converges towards zero. Figure 3.1 also shows the limit where the two-fluid model turns elliptical and ill-posed (assumed well-posed otherwise.) There is a region of positive wave growth within which the viscous model remains hyperbolic. No such region exists in the inviscid model.

## 4 Stability of Discrete Representations

We start the discrete analysis by examining the stability of representations of the two-equation model (2.3). The remarks that then follow relates these results to representations of the four-equation model (2.1). Let  $(\delta\psi)_j^n$  symbolize the discrete differentiation operations used in the discretization

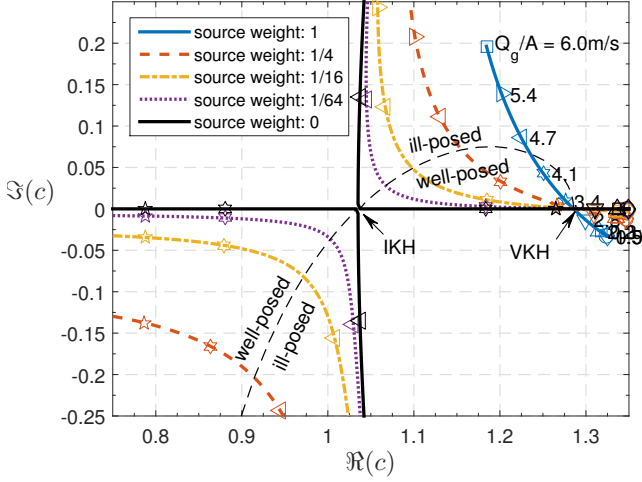


Figure 3.1: Complex celerity  $c$  with altering superficial gas velocity  $Q_g/A$ .  $Q_g$ ,  $A$  and the source differentials are kept constant about the critical VKH state. The source differentials are reduced in steps with a constant ‘source weight’ between plots. Parameter values are presented in Section 5.2

to represent the partial differentials. System (2.3) may be written

$$(\delta_t \mathbf{v})_j^n + (\delta_x \mathbf{f})_j = \nu (\delta_{xx} \mathbf{v})_j + \mathbf{s}_j \quad (4.1)$$

after discretization.  $\nu$  is here whatever artificial numerical viscosity one chooses to impose on the discretization. For example,  $\nu = \Delta x^2 / 2\Delta t$  and central differences for the spatial derivatives constitutes a Lax-Friedrich scheme.

First, let us regard the stability of (4.1) in the context of a common von Neumann analysis [VonNeumann and Richtmyer \[1950\]](#). Introduce  $\tilde{\mathbf{v}}_j^n = \mathbf{v}_j^n - \mathbf{V}$  and express  $\{\tilde{\mathbf{v}}_j^n\}$  and  $\{\tilde{\mathbf{v}}_j^{n+1}\}$  with spatial Fourier transforms

$$\tilde{\mathbf{v}}_j^n = \sum_k \hat{\mathbf{v}}_k^n e^{ikx_j}, \quad \tilde{\mathbf{v}}_j^{n+1} = \sum_k \hat{\mathbf{v}}_k^{n+1} e^{ikx_j}. \quad (4.2)$$

Insertion into (4.1) and dropping higher order terms yields a system on the form

$$\sum_k (\hat{\mathbf{v}}_k^{n+1} - \mathbb{G}_k \hat{\mathbf{v}}_k^n) e^{ikx_j} = \mathbf{0},$$

$\mathbb{G}$  being the amplification matrix. We have

$$\hat{\mathbf{v}}_k^{n+1} = \mathbb{G}_k \hat{\mathbf{v}}_k^n = \mathbb{G}_k \mathbb{G}_k \hat{\mathbf{v}}_k^{n-1} = (\mathbb{G}_k)^{n+1} \hat{\mathbf{v}}_k^0, \quad (4.3)$$

which provides the result of a common von Neumann analysis, namely that the spectral radius of  $\mathbb{G}_k$  must be less or equal to one as a necessary condition for system stability.

Rather than examining  $\mathbb{G}_k$ , we will use the continuous stability analysis from the previous section for which the solution is already calculated. Notice that the equation (4.2), once (4.3) is inserted, can be written on exactly the form

(3.3), provided  $\mathbb{G}_k$  is diagonalisable. In this case,  $\mathbb{P}$  contains the eigenvectors of  $\mathbb{G}_k$  and  $c_{k,p}^d = \frac{i}{k} \frac{\ln \lambda_{\mathbb{G}_k,p}}{\Delta t}$ ,  $\lambda_{\mathbb{G}_k,p}$  being the  $p$ -th eigenvalue of  $\mathbb{G}_k$ . In fact, this is a solution at any point in our discrete system for as long as non-linear effects remain negligible. Again, these are just linear combinations of modes; we may express the discrete point solution analogous to (4.4) by

$$\tilde{\mathbf{v}}_j^n = \sum_k \sum_{p=1,2} \hat{\mathbf{v}}_{k,p} e^{ik(x_j - c_{k,p}^d t_n)}. \quad (4.4)$$

Inserting (4.4) into the discrete model (4.1) and linearizing yields a system analogous to (3.5),

$$\sum_k \sum_{p=1,2} \frac{\partial \mathbf{E}_{k,p}^d}{\partial \mathbf{V}} \hat{\mathbf{v}}_{k,p} e^{ik(x_j - c_{k,p}^d t_n)} = \mathbf{0}, \quad (4.5)$$

$\mathbf{E}^d$  being the discrete equivalent of  $\mathbf{E}$  from (3.6), differing only in that discrete differential operators

$$\delta^d \equiv \frac{(\delta \exp ik(x - c^d t))_j^n}{\exp ik(x_j - c^d t_n)} \quad (4.6)$$

replace  $\delta$ . These  $\delta^d$  terms, approximating  $\delta$ , hold all numerical error in its entirety and are simple algebraic expressions. Again,  $\mathbf{E}^d$  is independent of  $n$  and  $j$  so that each  $k, p$ -term must equal zero individually. The problem is now equivalent to (3.7) and its solution is obtained directly from (3.13)-(3.15), with two celerities for each wavenumber  $k$ . Also the discrete viscous celerity  $c_\nu^d$  follow the definition (3.10) using the *discrete*  $\delta^d$  operators.  $\delta^d$  gives the value of  $\delta_t^d$ , which in turn gives the wave growth and dispersion from the chosen time discretization method. For example, the explicit or *forward Euler* time integration has the operator  $\delta_t^d = \frac{1}{\Delta t} (e^{-ikc^d} - 1)$ . Solving for  $c^d$  yields  $c^d = \frac{1}{k\Delta t} \ln(1 + \delta_t^d \Delta t)$  with  $\delta_t^d = \nu \delta_{xx}^d - c_\nu^d \delta_x^d$  from (3.10).<sup>2</sup>

$\delta^d$ -functions for some of the most common discrete differentiations are presented in Table 1. Tabulated operators are presented with phase angles  $\phi_x = k\Delta x$  and  $\phi_t = kc^d \Delta t$ , which represent the phase rotation within a grid cell length or time step, respectively. Constructing similar operators for more complicated interpolations is usually straight forward. For instance,  $\delta_x^d$  in the QUICK scheme is  $\frac{1}{8\Delta x} (3e^{i\phi_x} + 3 - 7e^{-i\phi_x} + e^{-i2\phi_x})$ . Notice that all operators listed in Table 1 are consistent, *i.e.*, they satisfy  $\delta^d \rightarrow \delta$  as  $\Delta x$  and  $\Delta t$  approach zero.

<sup>2</sup>We may generalize the discrete time differential operators listed in Table 1 by introducing the ‘degree of implicitness’  $r$  as a linear combination of the forwards and backwards Euler integrations,  $\frac{1}{\Delta t} (\psi^{n+1} - \psi^n) + r(\dots)^{n+1} + (1-r)(\dots)^n$ . The discrete differential operator for this integration is  $\delta_t^d = \frac{1}{\Delta t} \frac{\exp(-ikc^d) - 1}{r(\exp(-ikc^d) - 1) + 1}$ , giving  $c = \frac{1}{k\Delta t} \ln \left( \frac{1 + (1-r)\delta_t^d \Delta t}{1 - r\delta_t^d \Delta t} \right)$ .

			$(\delta\psi)_j^n$	$\delta^d$
$\delta_t$	$-ikc$	explicit	$\frac{1}{\Delta t}(\psi_j^{n+1} - \psi_j^n) + (\dots)^n$	$\frac{1}{\Delta t}(e^{-i\phi_t} - 1)$
$\delta_t$	$-ikc$	implicit	$\frac{1}{\Delta t}(\psi_j^{n+1} - \psi_j^n) + (\dots)^{n+1}$	$\frac{1}{\Delta t}(1 - e^{i\phi_t})$
$\delta_t$	$-ikc$	Crank-Nicolson	$\frac{1}{\Delta t}(\psi_j^{n+1} - \psi_j^n) + \frac{1}{2}(\dots)^{n+1} + \frac{1}{2}(\dots)^n$	$\frac{2i}{\Delta t} \tan \frac{\phi_t}{2}$
$\delta_x$	$ik$	upwind	$\frac{1}{\Delta x}(\psi_j - \psi_{j-1})$	$\frac{2i}{\Delta x} \sin \frac{\phi_x}{2} e^{-i\frac{\phi_x}{2}}$
$\delta_x$	$ik$	central difference	$\frac{1}{2\Delta x}(\psi_{j+1} - \psi_{j-1})$	$\frac{i}{\Delta x} \sin \phi_x$
$\delta_x$	$ik$	staggered	$\frac{1}{\Delta x}(\psi_{j+\frac{1}{2}} - \psi_{j-\frac{1}{2}})$	$\frac{2i}{\Delta x} \sin \frac{\phi_x}{2}$
$\delta_{xx}$	$-k^2$	central difference	$\frac{1}{\Delta x^2}(\psi_{j+1} - 2\psi_j + \psi_{j-1})$	$\frac{2}{\Delta x^2}(\cos \phi_x - 1)$
$\bar{\psi}_j$	$\Psi$	mean	$\frac{1}{2}(\psi_{j+\frac{1}{2}} + \psi_{j-\frac{1}{2}})$	$\cos \frac{\phi_x}{2}$

Table 1: Some discrete differentiation operators and their corresponding wave operator.  $\phi_x = k\Delta x$  and  $\phi_t = kc\Delta t$ .

**Remark 1.** *The stability behaviour of a discrete representation will converge towards that of the continuous model if*

$$c_\nu^d \equiv -\frac{\delta_t^d - \nu\delta_{xx}^d}{\delta_x^d} \rightarrow c + ik\nu.$$

For this to happen, all  $\delta^d$  operators must be consistent ( $\delta^d \rightarrow \delta$ ) and  $\Delta x$  and  $\Delta t$  must approach zero together, smoothly.

**Remark 2.** *The predicted linear stability is independent of which variable the discrete system is solved for, provided the discrete differentiations  $\delta^d$  are independent of this choice.*

**Remark 3.** *The predicted linear stability is independent of the form of the discrete system, be it conservative, primitive, four-equation, two-equation, etc., provided the discrete differentiations  $\delta^d$  are independent of these choices.*

Remark 2 and 3 are results of the linearisation. This is briefly illustrated by Taylor expanding any chosen variable  $v(w)$  about  $\mathbf{W}$  which yields

$$\tilde{v} = \mathbf{V} + \frac{\partial \mathbf{V}}{\partial \mathbf{W}} \tilde{\mathbf{w}} + \mathcal{O}(|\tilde{\mathbf{w}}|^2),$$

where  $\mathbf{V} = v(\mathbf{W})$ . We may thus define

$$\tilde{\mathbf{w}} \equiv \frac{\partial \mathbf{W}}{\partial \mathbf{V}} \tilde{v}$$

and freely impose variable transformations which does not affect the linear stability of the system, provided those transformation matrices exist.

Further, in linearizing an arbitrary discretized variable  $w$ , and remembering that  $(\delta \mathbf{W})_j^n = 0$ , one finds

$$(\delta w)_j^n \rightarrow \delta^d \tilde{\mathbf{w}} = \frac{\partial \mathbf{W}}{\partial \mathbf{V}} \delta^d \tilde{v}.$$

The linear system of one variable will thus only be a factorization of the same system in another variable, as alluded to in Remark 2. Also noted in the remark,  $\delta^d$  must be unchanged in the variable transformation of the last equality.

Finally, any type term representation based on the chain rule will, after the linearization, be equivalent. For example

$$\left(\frac{\partial f}{\partial w}\right)_j^n (\delta w)_j^n \rightarrow \left(\frac{\partial \mathbf{F}}{\partial \mathbf{W}} + \mathcal{O}(\tilde{\mathbf{w}})\right) \delta^d \tilde{\mathbf{w}} = \delta^d \tilde{\mathbf{f}}.$$

Any discrete representation of system 2.1 will thus be equivalent, provided the discrete differential operators  $\delta_t^d$ ,  $\delta_x^d$  and  $\delta_{xx}^d$  are respectively the same.

A consequence of Remark 3 is that four equation formulations of the compressible system (2.1) is equivalent to (4.1) provided we do not mix different discrete differentiations. Examples of commonly used mixed discrete differentiations are convection flux terms of the form

$$(\psi u)_{j+\frac{1}{2}} = \begin{cases} \psi_j \bar{u}_{j+\frac{1}{2}} & \text{if } \bar{u}_{j+\frac{1}{2}} \geq 0, \\ \psi_{j+1} \bar{u}_{j+\frac{1}{2}} & \text{otherwise,} \end{cases}$$

(which linearizes to a central difference in  $\tilde{u}$  and an upwind difference in  $\tilde{\psi}$ .) Staggered grid formulations, in which the differentiation depends on the proximity of the data points, is another example.

Incompressible fluids are assumed in the stability analysis itself in the present work, even though the representation is of the compressible model. This is common practise and provides us with simple, explicit stability expressions, though denies us information about the sonic stability. Including density variations is straightforward, but necessitates solving a higher order dispersion equation numerically.

**Example 1** (The stability of a Lax-Friedrich and a local Lax-Friedrich scheme). *The Lax-Friedrich scheme is commonly written*

$$\frac{v^{n+1} - v^n}{\Delta t} + \frac{f_{j+\frac{1}{2}} - f_{j-\frac{1}{2}}}{\Delta x} = s_j$$

with

$$f_{j+\frac{1}{2}} = \frac{1}{2}(f_{j+1} + f_j) - \frac{\nu}{\Delta x}(v_{j+1} - v_j).$$

*Numerical viscosities in the Lax-Friedrich scheme and the local Lax-Friedrich scheme are then*

$$\nu^{\text{LF}} = \frac{\Delta x^2}{2\Delta t} \quad \text{and} \quad \nu^{\text{LLF}} = \frac{\Delta x}{2} \max |\lambda^\pm|,$$

*respectively. Thus, the local Lax-Friedrich scheme determines the artificial numerical diffusion according to spectral*

radius of  $\frac{\partial f}{\partial v}$ . Eigenvalues, presented in (2.6), are computed at the steady state  $\mathbf{v} = \mathbf{V}$ .

These schemes use simple central differences; from Table 1 we find  $\delta_x^d = \frac{i}{\Delta x} \sin \phi_x$  and  $\delta_{xx}^d = \frac{2}{\Delta x^2} (\cos \phi_x - 1)$ . Extracting the stability equations of either scheme is strikingly easy; equation (3.17) gives  $c_\nu^d$ ,  $\delta_t^d$  is obtained from the definition (3.10) and the complex wave celerity from the expression of the chosen time discretization.

**Example 2** (The stability of a scheme for the compressible model on a staggered grid). Say we wish to simulate the compressible model (2.1) with a staggered grid discretizations. Staggered grids are quite common with this model as the staggered grid offers a tight stencil for most of the data points and denies so-called checkerboard solutions of the pressure field (see e.g. Ferziger and Peric [1999].)

Upper-case indices  $J$  are used for the mass control volume centre points, and lower-case indices  $j$  for the momentum ones. The staggered grid is constructed with the momentum control volumes shifted spatially half a cell length behind the mass control volumes, i.e.,  $x_j = x_J - \frac{1}{2}\Delta x$ , as illustrated in Figure 4.1.



Figure 4.1: The staggered grid; cells and indices.

As opposed to on a co-located grid (non-staggered,) the orientation of the data points is likely to affect the way in which individual terms are discretized, and therefore also the stability behaviour. A particular choice has therefore been made for the variables of this example, namely physically conserved variables of specific mass  $\rho a_\kappa = \rho_\kappa a_\kappa$  and specific momentum  $\rho q_\kappa = \rho_\kappa q_\kappa$ . A sensible discretization can be written

$$\begin{aligned} (\delta_t \rho a_\kappa)_j^n + (\delta_x \rho q_\kappa)_j^n &= \nu (\delta_{xx} \rho a_\kappa)_j^n \\ (\delta_t \rho q_\kappa)_j^n + (\delta_x (\rho q u)_\kappa)_j^n + \overline{a_{\kappa,j}} (\delta_x p)_j^n + g_y \overline{\rho a_{\kappa,j}} (\delta_x h)_j^n \\ &= \nu (\delta_{xx} \rho q_\kappa)_j^n + s_{\kappa,j}, \\ a_{\ell,J} + a_{g,J} &= \mathcal{A}, \quad a_{\kappa,J} = \frac{\rho a_{\kappa,J}}{\rho_{\kappa,J}}, \end{aligned}$$

with

$$\begin{aligned} p_J &= \mathcal{P}(\rho a_{\ell,J}, \rho a_{g,J}), \\ h_J &= \mathcal{H}(a_{\ell,J}), \\ s_{\kappa,j} &= \mathcal{S}_\kappa \left( \overline{a_{\kappa,j}}, \frac{\rho q_{\ell,j}^n}{\rho_{\ell,j}}, \frac{\rho q_{g,j}^n}{\rho_{g,j}} \right), \end{aligned}$$

and arithmetic averaging

$$\overline{w}_j = \frac{1}{2} (w_J + w_{J-1})$$

being used in between data points. The momentum convection term  $(\delta_x (\rho q u)_\kappa)_j^n$  is for now kept purely symbolic. Compressibility effects are dismissed in the linear analysis and densities again made constant, as in all VKH analyses.

The discrete pressure differential  $(\delta_x p)_j^n$  can again be eliminated between the momentum equations after dividing each by  $\overline{a_{\kappa,j}}$ . Thus, a Fourier solution on the form (4.4) once more yields a linearized system similar to (4.5), but with the variables  $\tilde{\mathbf{w}} = (\tilde{a}_\ell, \tilde{a}_g, \tilde{q}_\ell, \tilde{q}_g)^T$ . The system reads

$$\frac{\partial \mathbf{E}^d}{\partial \mathbf{W}} \tilde{\mathbf{w}} = \begin{pmatrix} -c_\nu^d \hat{a}_\ell + \delta_x \hat{q}_\ell \\ -c_\nu^d \hat{a}_g + \delta_x \hat{q}_g \\ \left[ \frac{\rho}{A} \left( -c_\nu^d \hat{q} + \widehat{\delta_x^d q u} \right) \right]_\ell + m_y \mathcal{H}' \delta_x^d \hat{a}_\ell \\ -\hat{a}_\ell \cos \frac{\phi_x}{2} \mathcal{S}_{A_\ell} - \hat{q}_\ell \mathcal{S}_{Q_\ell} - \hat{q}_g \mathcal{S}_{Q_g} \\ \hat{a}_\ell + \hat{a}_g \end{pmatrix}$$

with  $[\cdot]_\ell = (\cdot)_\ell - (\cdot)_g$ . The tight stencil reduces the error in the  $\delta_x^d$  operator to  $\delta_x^d = \frac{2i}{\Delta x} \sin \frac{\phi_x}{2}$  for those data points located favourably on the staggered grid. In this case only the momentum convection term requires an alternative form of spacial differencing. We split it into  $\hat{a}_\kappa$  and  $\hat{q}_\kappa$  components and define  $\delta_{a,x}^d$  and  $\delta_{q,x}^d$  by

$$\widehat{\delta_x^d (q u)}_\kappa = 2U_\kappa \delta_{q,x}^d \hat{q}_\kappa - U_\kappa^2 \delta_{a,x}^d \hat{a}_\kappa$$

so that the term become analogues to the previous examples.

The simplest approach is to take the determinant of  $\frac{\partial \mathbf{E}^d}{\partial \mathbf{W}}$ , requiring it to be zero for every wavenumber. A discrete version of (3.13) then emerges with

$$\begin{aligned} J'_{r,d} &= m_y \mathcal{H}' - \left( \rho \left( U^2 \frac{\delta_{a,x}^d}{\delta_x^d} - 2U c_\nu^d \frac{\delta_{q,x}^d}{\delta_x^d} + c_\nu^{d2} \right) \right)^*, \\ S'_d &= \cos \frac{\phi_x}{2} \mathcal{S}_{A_\ell} + c_\nu^d (\mathcal{S}_{Q_\ell} - \mathcal{S}_{Q_g}). \end{aligned}$$

$J'_{r,d}$  is of course identical in form to (3.14) if  $\delta_{a,x}^d = \delta_{q,x}^d = \delta_x^d$ , and  $S'_d$  to (3.15) if not for the arithmetic average, as pointed out in Remark 3.

An upwind-type interpolation may be chosen for the momentum convection term to complete the example. If we choose, say,

$$(\delta_x (\rho q u)_\kappa)_j^n = \frac{1}{\Delta x} (\rho a_{\kappa,J} \overline{u_{\kappa,j}}^2 - \rho a_{\kappa,J-1} \overline{u_{\kappa,j-1}}^2),$$

with  $\overline{u_{\kappa,j}} = \rho q_{\kappa,j} / \overline{a_{\kappa,j}}$ , we get

$$\begin{aligned} \delta_{a,x}^d &= \frac{2i}{\Delta x} \left( e^{-i \frac{\phi_x}{2}} \sin \phi_x - \sin \frac{\phi_x}{2} \right), \\ \delta_{q,x}^d &= \frac{2i}{\Delta x} e^{-i \frac{\phi_x}{2}} \sin \frac{\phi_x}{2}. \end{aligned}$$

This is a rather diffusive choice, made to stabilize the scheme as the staggered conservative variable formulation turns out to provide very little diffusion otherwise. Solving for other variables, such as phase fractions and velocities, is also quite common and would entail other differentiations and result in a different dispersion equation. One may for example look to the example in Liao et al. [2008], although this example appear to neglect that some of the information in the momentum equation is dislocated.

**Example 3** (The Stability of a Roe Scheme). The Roe scheme is presented in A. A viscous matrix, the Roe matrix,

is used in this scheme in place of a scalar viscosity. Let's split it into a diagonal part and an off-diagonal part:

$$\frac{\Delta x}{2} \mathbb{L}^{-1} |\Lambda| \mathbb{L} = \nu \mathbb{I} + \nu_{\text{T}} \begin{pmatrix} 0 & 1/\varkappa \\ \varkappa & 0 \end{pmatrix}$$

where

$$\nu = \frac{\Delta x}{2} \frac{1}{2} (|\lambda^+| + |\lambda^-|), \quad \nu_{\text{T}} = \frac{\Delta x}{2} \frac{1}{2} (|\lambda^+| - |\lambda^-|)$$

Following the previous procedure, we regain the form (3.13), but with

$$J'_{\text{r,d}} = \frac{(\gamma \varkappa)^2 - ((\rho U_{\text{r}})^*)^2}{\rho^*} = m_{\text{y}} \mathcal{H}' - (\rho U_{\text{r}}^2)^* - \frac{1 - \gamma^2}{\rho^*} \varkappa^2,$$

$$S'_{\text{d}} = \gamma \mathcal{S}_{A_{\ell}} + c_{\nu, \nu_{\text{T}}}^{\text{d}} (\mathcal{S}_{Q_{\ell}} - \mathcal{S}_{Q_{\text{g}}}),$$

where

$$\gamma = 1 - \nu_{\text{T}} \frac{\rho^* \delta_{xx}^{\text{d}}}{\varkappa \delta_x^{\text{d}}} \quad \text{and} \quad c_{\nu, \nu_{\text{T}}}^{\text{d}} = c_{\nu}^{\text{d}} - \nu_{\text{T}} \frac{(\rho U)^* \delta_{xx}^{\text{d}}}{\varkappa \delta_x^{\text{d}}}.$$

Central difference operators  $\delta_x^{\text{d}} = \frac{i}{\Delta x} \sin \phi_x$ ,  $\delta_{xx}^{\text{d}} = \frac{2}{\Delta x^2} (\cos \phi_x - 1)$  are again implied. The viscous terms will disappear from  $c_{\nu, \nu_{\text{T}}}^{\text{d}}$  if both characteristics are of the same sign; the predicted wave celerity will be very precise as the flow turns unstable.

In fact, because  $\mathbb{L}^{-1} |\Lambda| \mathbb{L}$  equals the Roe matrix  $\left( \frac{\partial \mathbf{F}}{\partial \mathbf{V}} \right)^{\text{Roe}}$  from (A.1) if both eigenvalues are positive, and  $-\left( \frac{\partial \mathbf{F}}{\partial \mathbf{V}} \right)^{\text{Roe}}$  if both eigenvalues are negative, and because the Roe matrix is designed to obey

$$\left( \frac{\partial \mathbf{F}}{\partial \mathbf{V}} \right)^{\text{Roe}}_{j+\frac{1}{2}} (\mathbf{v}_{j+1} - \mathbf{v}_j) = \mathbf{f}_{j+1} - \mathbf{f}_j,$$

the stability of the Roe scheme (A.2) is identical to that of the simple upwind scheme

$$\mathbf{f}_{j+\frac{1}{2}} = \begin{cases} \mathbf{f}_j, & \lambda^+ > 0, \lambda^- > 0 \\ \mathbf{f}_{j+1}, & \lambda^+ < 0, \lambda^- < 0 \end{cases} \quad (4.7)$$

in the case of supercritical flow. Then, the growth and celerity equations once more reduce to (3.17) with the upwind differentiation  $\delta_x^{\text{d}} = \frac{1}{\Delta x} (1 - e^{-i\phi_x}) = \frac{2i}{\Delta x} \sin \frac{\phi_x}{2} e^{-i\frac{\phi_x}{2}}$  and no net artificial viscosity;  $\nu = 0$ .

Equation (3.16) reveals that the VKH criterion (3.18), where wave growth is at an equilibrium with  $c = c_{\text{crit}} \in \mathbb{R}$ , coincides with hydraulically critical flow relative to the perturbation wave. That is, one of the relative eigenvalues  $\lambda_{\text{T}}^{\pm} = \lambda^{\pm} - c$  equals zero at neutral stability. This means that the Roe scheme is equivalent to (4.7) whenever the VKH wave growth is positive.

## 5 Numerical Tests and Results

Predictions from a number of schemes will here be presented, namely the explicit and implicit variants of the Lax-

Friedrich scheme (Example 1), abbreviated LF, the staggered upwind scheme solved for conservative variables (Example 2), abbreviated UWS, and the Roe scheme (Example 3.) The aim of these comparisons is not to establish a favourite amongst the chosen representations, but to demonstrate how the linear theory provides a powerful simulation support tool. Indeed, multiple considerations are important when choosing a scheme. Many choices can be made both stable and accurate if the simulation parameters are collected with the aid of the hitherto presented linear theory.

### 5.1 Initial Conditions

Disregarding compressibility, the flow development that springs out from the initial conditions will generally consist of two waves per wavenumber, as given in the solution (3.4) or (4.4). These solutions show that  $\hat{\mathbf{v}}_k^0 = \sum_p \hat{\mathbf{v}}_{k,p}$ , each  $\hat{\mathbf{v}}_{k,p}$  superimposing one of the two  $c_{k,p}$  waves. In order for a simulation to provide only a single wave  $c_{k_1, p_1}$  the initial conditions must be  $\hat{\mathbf{v}}_{k_1}^0 = \hat{\mathbf{v}}_{k_1, p_1}$ ,  $\hat{\mathbf{v}}_{k \neq k_1}^0 = 0$ , where  $\hat{\mathbf{v}}_{k_1, p_1}$  satisfies (3.7). This was implicitly carried through in the VKH derivation of Section 3 by the transformation  $\frac{\partial \mathbf{V}}{\partial A_{\ell}} \hat{a}_{\ell} = \hat{\mathbf{v}}$ , which revealed (3.12). (3.12) implies the transformation  $\frac{\partial \mathbf{V}}{\partial A_{\ell}} = (1, -(\rho U_{\text{r}})^*)^T$ . Thus, after choosing a volumetric disturbance  $\hat{a}_{\ell, k_1}$ , a pure  $c_{k_1, p_1}$  disturbance wave is obtained by choosing

$$\hat{\mathbf{v}}_{2, k_1}^0 = [\rho \hat{u}]_{\text{g}}^{\ell} = -(\rho(U - c_{\nu, k_1, p_1}^{\text{d}}))^* \hat{a}_{\ell, k_1}^0. \quad (5.1)$$

Corresponding primitive variables  $\hat{u}_{\kappa}$  are found from the transformation matrix (B.1b).

Figure 5.1 shows a single wavelength  $\hat{a}_{\ell, k_1}^0$ , simulated twice with an explicit, non-staggered Lax-Friedrich scheme. First, the initial perturbation is applied only to the phase fraction, i.e.,  $\hat{u}_{\kappa, k}^0 \equiv 0$ . Expression (5.1) is used for the phase velocities in the second simulation. After a short transition period where both waves interact, the fast wave is seen to dominate the growth of the first simulation. No transition period is observed in the second simulation. Indeed, Liao et al. [Liao et al. [2008]] demonstrated that the wave growth of a simulation with fairly random initial conditions quickly turns independent of these and develops according to the dominant wavelength. A figure similar to 5.1 is also presented in Brook et al. [1999/10/10] for gravity driven flows in collapsible tubes.

### 5.2 Test Case

The setup for the computational examples will now be presented. This setup is chosen fairly arbitrarily and corresponds to the experimental and numerical setup used in Holmås [2010], Johnson [2005], Akselsen [2016a,b]. The friction closures  $\tau_{\kappa}$  and  $\tau_1$  are from the Biberg friction model as presented in Biberg [2007], also described in the other citations just mentioned. Fixed parameters are presented in Table 2 unless otherwise stated and constitutes a high-pressure, positively inclined flow. The flow state is chosen



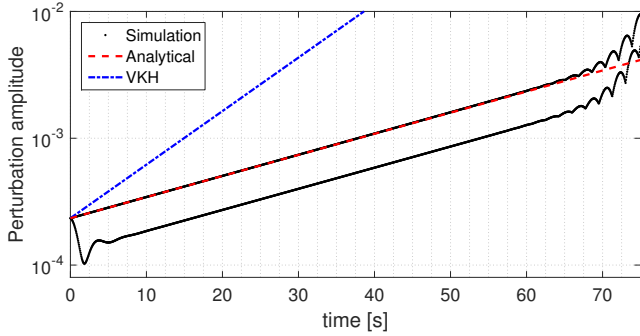


Figure 5.1: Perturbation wave amplitude  $\max_j \{\tilde{a}_{\ell,j}^n\} / \mathcal{A}$  vs. time.

Comparing single wave simulation with initial conditions  $\hat{\mathbf{v}}_{k_1}^0 = (\hat{a}_{\ell,k_1}^0, 0)^T$  (plot with initial disturbance) to simulation with initial conditions from (5.1) (plot without initial disturbance); explicit Lax-Friedrich simulation.

such that the flow is weakly unstable according the differential VKH criterion. Truly fixed flow parameters in the incompressible flow simulations are the steady state level height  $\bar{h} = 0.2d$  and mixture velocity  $Q/\mathcal{A} = 3.4\text{m/s}$ . The equivalent mean liquid area fraction is  $A_\ell/\mathcal{A} = 0.142$  and the chosen friction closures will yield the steady state superficial velocities  $Q_\ell/\mathcal{A} \approx 0.154\text{m/s}$  and  $Q_g/\mathcal{A} \approx 3.245\text{m/s}$ . The overall properties of the friction closure does not affect the linear stability analysis; only their resulting steady state  $S = 0$  and its state derivatives enter into it. In this particular case we have  $S_{A_\ell} = 1.39\text{E}6\text{ kg/m}^6\text{s}^2$ ,  $S_{Q_\ell} = -9.07\text{E}5\text{ kg/ms}$  and  $S_{Q_g} = 7.63\text{E}4\text{ kg/ms}$ .

Only numerical parameters are varied in the tests provided in this section. The wavelength is therefore fixed at 30 diameters and the cell lengths are varied. Of course, doing it the other way around would also be insightful, showing which wavelengths one can expect to see on any given grid arrangement.

liquid density	$\rho_\ell$	998	$\text{kg/m}^3$
gas density	$\rho_g$	50	$\text{kg/m}^3$
liquid dynamic viscosity	$\mu_\ell$	1.00E-3	$\text{Pa s}$
gas dynamic viscosity	$\mu_g$	1.61E-5	$\text{Pa s}$
internal pipe diameter	$d$	0.1	$\text{m}$
wall roughness		2E-5	$\text{m}$
pipe inclination	$\theta$	1°	—
mean level height	$\bar{h}$	0.02	$\text{m}$
mixture velocity	$Q/\mathcal{A}$	3.4	$\text{m/s}$
wavelength	$\lambda$	3	$\text{m}$

Table 2: Fixed parameters.

The time steps are regulated using a CFL number, which makes the time step length proportional to the grid cell length (see Remark 1.) The spectral radius will typically be used for selecting the time step length in schemes where the characteristic information is computed, and the CFL number chosen close to unity;  $\Delta t = \text{CFL} \Delta x / \max_{j,\pm} |\lambda_j^\pm|$  with

$\text{CFL} = 0.95$  has been adopted in the presented Roe and local Lax-Friedrich schemes. One of the phase velocities is commonly used in schemes not based on the model eigenstructure. Following Liao et al. [2008], the liquid velocity is chosen to limit the time step for the staggered upwind and Lax-Friedrich schemes,  $\Delta t = \text{CFL} \Delta x / \max_j |u_{\ell,j}|$ , with  $\text{CFL} = 0.5$ . Implicit scheme simulations are performed by iterating on the new state with a 0.5 relaxation factor.

### 5.3 Predictions

First, Figure 5.2 validates that the theory corresponds precisely to the linear growth of the discrete representations and shows the further development into the non-linear range. The simulation domain here consists of 128 cells containing a single wave of the prescribed 30 diameter wavelength. Subfigure (a) show the wave growth by logarithmically plotting the largest liquid fraction amplitudes. The spatial locations of the wave crest peaks are plotted in Subfigure (b), providing the wave speed. Initial conditions are set to accommodate the most unstable wave, which is in these cases the fast wave.

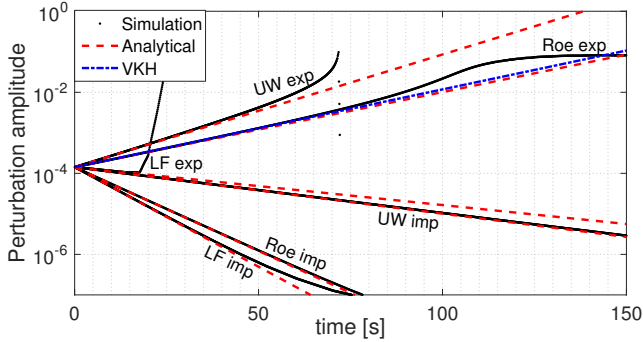
The presented schemes provide a range of different behaviours. We note immediately from Figure 5.2a that all implicit schemes are significantly more diffusive than their explicit counterparts, with numerical diffusion dominating the weak wave growth present in the differential solution. Explicit versions of both the Lax-Friedrich scheme and the staggered upwind scheme eventually reach a final unstable state in which waves grow until the model is no longer hyperbolic and simulations crash. They do so, however, in quite different manners. Where the Lax-Friedrich scheme first appears diffusive for then to be dominated by a high-wavenumber instability, the upwind scheme simply overpredicts the growth rate of the principle wave. This is further illustrated in Figure 5.3, showing growth rates and snapshots of simulations in which the differential model is stable due to a lower mixture velocity. The former instability will usually be regarded as a ‘numerical instability,’ commonly identified by the sudden unphysical high-wavenumber growth. Determining, from visual inspection, whether the latter instability is ‘physical or not’ is however not as straight forward as there are essentially no differences between the natural wave growth and the growth here attributed to numerical errors.

Lastly, the explicit Roe scheme is in Figure 5.2a seen to accurately match the continuous growth rate of the differential model. It also develops into a steady roll-wave solution, which is a valid solution for the differential problem (see Akselsen [2016a];) Roe schemes are designed to be well adopted for strongly non-linear flows.

The dispersion error of a 128 cell wave is very small, as seen in Figure 5.2b; wave crest positions are overlapping for as long as the waves remain in the linear range.

Next we examine the response of the 30 diameter wave to changes in the spatial resolution. Figure 5.4 shows the wave growth, or *pulsation*,  $k \Im(c^d) [1/\text{s}]$  and the wave celerity

(a) Wave growth: Perturbation wave amplitude  $\max_j \{\tilde{a}_{\ell,j}^n\} / A$  vs. time.



(b) Wave celerity: Perturbation peak location vs. time.

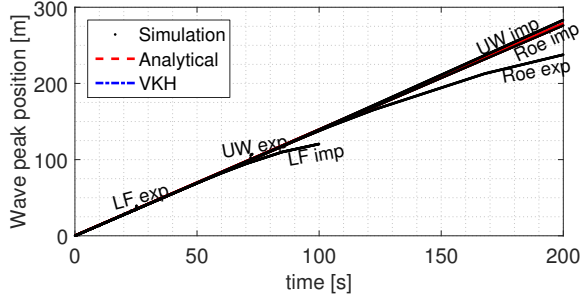


Figure 5.2: Numerical simulations vs. linear theory. Wave-length 30  $d$ . 128 cells;  $\phi_x = \pi/64$ .

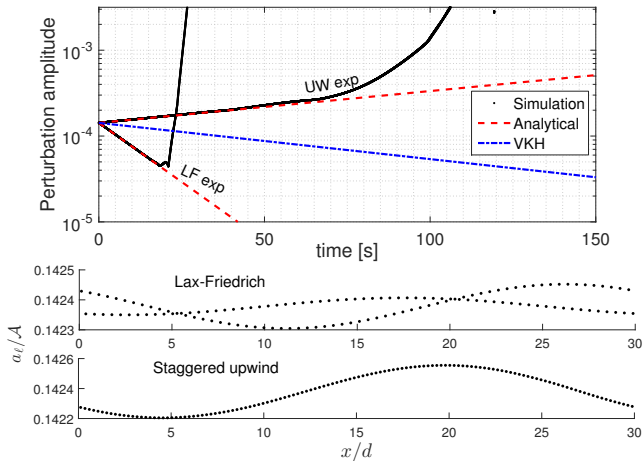


Figure 5.3: Wave growth and accompanying snapshots from unstable Lax-Friedrich and staggered upwind simulations. The mixture velocity  $Q/A$  equals here 3.1 m/s, at which the differential model is stable.

$\Re(c^d)$  [m/s]. Both the fast and the slow waves are shown, a bold line used for the wave with the higher growth rate. Subfigure (a) shows that the Roe scheme gives very accurate growth results for  $\phi \leq \pi/32$  (using 64 cells or more) and predicts wave growth for all  $\phi$ . An accurate celerity for the fast wave is observed in Subfigure (b) for all  $\phi$ . The explicit Lax-Friedrich and implicit staggered upwind schemes start predicting wave growth around  $\phi = \pi/100$ , and the implicit Roe and implicit Lax-Friedrich schemes start doing so around  $\phi = \pi/210$ . The explicit upwind scheme overpredicts the wave growth everywhere above  $\phi = \pi/3$ . Finally, we see that the explicit Lax-Friedrich scheme becomes unstable around  $\phi \gtrsim \frac{2}{3}\pi$ , and that it is then the slow wave that has taken over the growth. In fact, from Subfigure (b) we see that the ‘slow’ wave moves faster here. This very particular finding is tested and confirmed in Figure 5.5, where three-celled waves ( $\phi_x = \frac{2}{3}\pi$ ) are applied as the initial condition. Two simulations are shown wherein the initial velocity condition (5.1) is made to accommodate the fast wave in one and the slow wave in the other. The simulations follow the predicted growth behaviour precisely, with the slow wave growing and the fast wave diminishing. After a while though, also the fast wave simulation becomes unstable as the slow wave grows from out of numerical inaccuracies. The plotted points are the maximum amplitudes of the spatial node sets; there is some scattering of these points as the simulated waves are represented by a regularly alternating three-point pattern.

Next we look at how the discrete representations respond to changes in the time step. We have already observed that there is a significant difference in the stability and diffusivity of explicit and implicit time step integration. A strong time step dependence was also noted in Akselsen [2016a] for both linear and non-linear wave simulations. Figure 5.6 shows the wave growth and wave celerity as functions of the CFL number. Time steps  $\Delta t$  are selected on the basis of these as per the individual method descriptions, *i.e.*, based on the spectral radius  $\max |\lambda^\pm|$  in the Roe schemes and on the liquid velocity  $u_\ell$  in the Lax-Friedrich and upwind schemes.

We first note that the explicit and implicit versions of all schemes converge towards the same growth and celerity as the CFL number approaches zero, except for the Lax-Friedrich scheme whose numerical diffusion is inversely proportional to the time step length and thus approaches infinity with reducing CFL number. Growth increases ‘with increasing explicitness’ for the Roe and upwind scheme. As noted in Akselsen [2016a], growth predictions seems to be accurate in explicit schemes based on characteristic information, in this case the Roe scheme, as the CFL number nears unity. An interpretation of why this is is shown in Figure 5.7; information from the upwind mean state would spread nicely over the cell face during the time step limited by  $\text{CFL} \approx 1$ . This is particularly so if the cell face fluxes are dominated by information travelling along the path of the quickest characteristic, which seem to be case for supercritical flows.

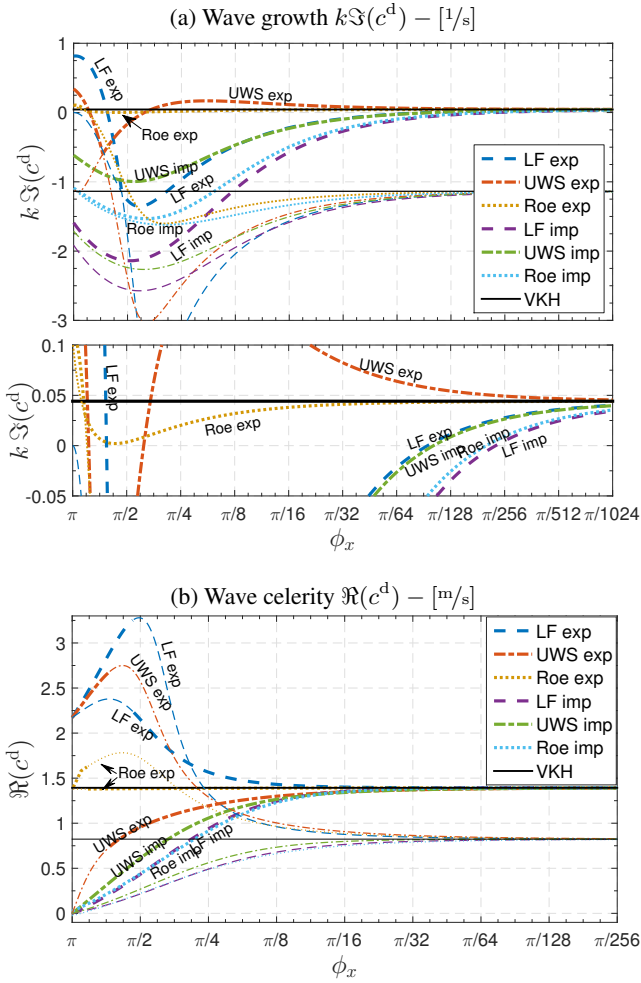


Figure 5.4: Linear theory with varying cell lengths  $\Delta x$ . 30  $d$  wavelength.  $\phi_x = k \Delta x = 2\pi/(\# \text{ cells in a wave})$

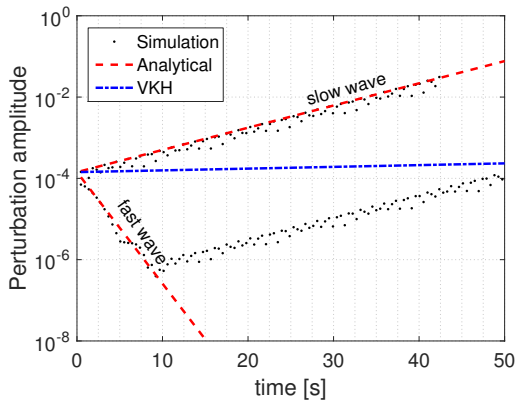


Figure 5.5: Explicit Lax-Friedrich scheme. Three cells per wave;  $\phi_x = \frac{2}{3}\pi$ .

The celerity graphs shown in Figure 5.6b show that the wave celerity of the Roe scheme becomes increasingly accurate as the time step is reduced. Indeed, the Roe scheme is designed to provide the accurate shock speeds for non-linear problems. Both centred schemes (Roe and Lax-Friedrich) provide better estimates of the wave celerity than the upwind scheme, whose dispersion error is mostly caused by the  $e^{-i\phi_x/2}$  term generated by the spatially asymmetric upwind formulation.

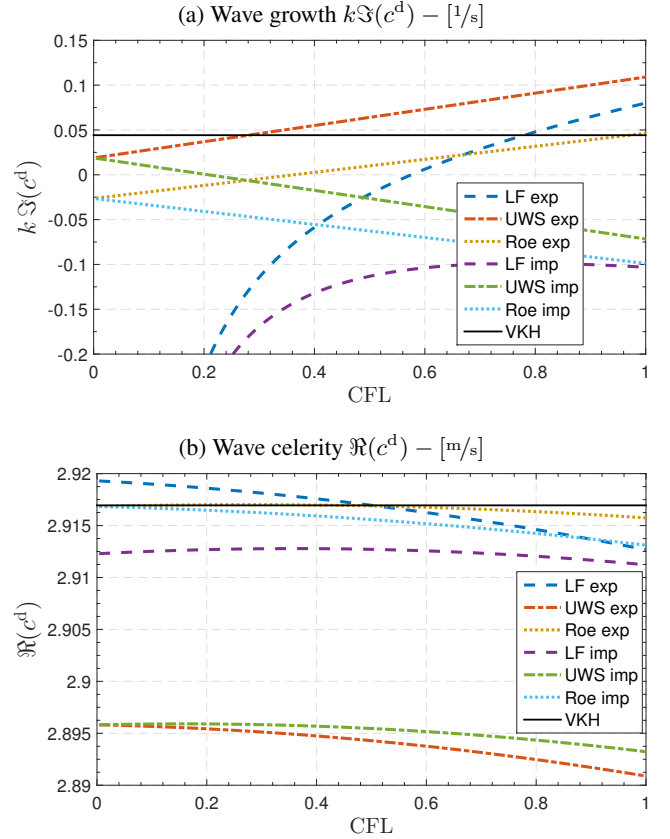


Figure 5.6: Linear theory with varying CFL number, showing the fast wave. 128 celled wave;  $\phi_x = \pi/64$

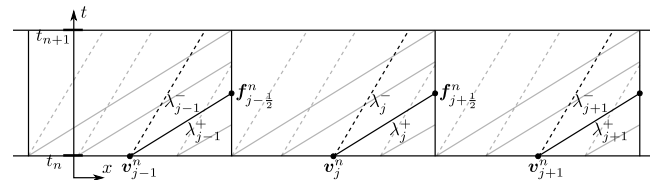


Figure 5.7: Sketch of the characteristic paths at CFL = 1

An alternative way of presenting the schemes' ability to predict wave growth is through a flow map such as that presented in Figure 5.8. This map is of the same 30 diameter wave with 128 cells ( $\phi_x = \pi/64$ ), and the flow rates are now varying. The CFL-numbers are specified as before and a root searcher is employed to identify the critical point. Numerically searching for the critical state

makes this form of visualization more computationally costly than the other plots presented in this section, which were all explicitly computed. Note that Equation (3.18) is not valid in the discrete representations because  $c_v^d$  does not equal  $c^d$ . A consequence is that the marginal stability of a discrete representation is wavelength dependent, while the marginal stability of the differential model is not.

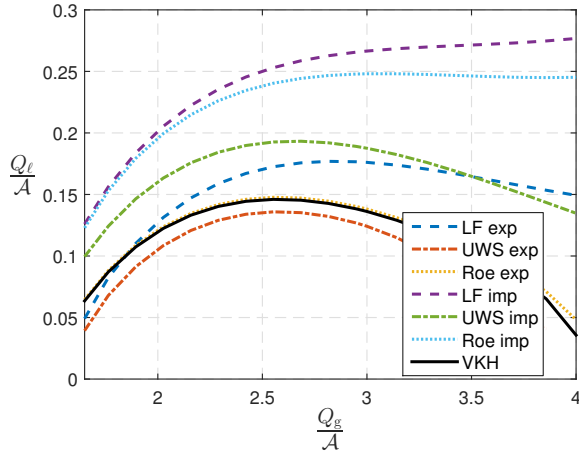


Figure 5.8: Flow map predicted by various schemes.  $\phi_x = \pi/64$ .

The local Lax-Friedrich scheme, not included amongst the presented results, gave growth results nearly identical to that of the Roe scheme all over. This indicates that it is the characteristic information in the viscous term and time step, rather than the off-diagonal contribution, that accounts for the favourable growth results of the Roe scheme. The local Lax-Friedrich scheme does however not converge as precisely with respect to the wave celerity  $\Re(c^d)$  as the Roe scheme, slightly underpredicting the fast celerity in plots similar to those of Figure 5.4b and 5.6b. This scheme was also seen to have the same type of slow wave instability near  $\phi = \pi$  as the simple Lax-Friedrich scheme.

So how does the time integration affect the stability and diffusivity of our solution? Let us examine the influence of the time discretization on a centred, non-staggered scheme without artificially added viscosity (using  $\nu = 0$  in the Lax-Friedrich scheme.) Such a scheme, though on a staggered grid, was in Liao et al. [2008] deemed the most accurate amongst those tested. Figure 5.9 shows the growth rates and wave celerities of this centred scheme with an explicit and implicit time integration, the liquid velocity based CFL number equalling 0.5. The curves for when the time step approaches zero are also shown. Note first that the high-wavenumber slow-wave instability of the explicit Lax-Friedrich scheme is not present here, attributing that phenomenon to the artificial viscosity  $\nu$ . The growth rates of the fast wave in Subfigure ((a)) are near mirror images of each other, the numerical error being predominantly attributed to the time step integration. This is important to be aware of;

numerical diffusion errors are often thought of as a symptom of the *spatial* discretisation alone.

If the wave growth in this example is dominated by the time integration then we would expect accurate growth results for small time steps  $\Delta t$ . In fact, since  $\delta_x^d = \frac{i}{\Delta x} \sin \phi_x$  is purely imaginary, examining the dispersion equation (3.13)-(3.15) reveals that  $c_v^d$  equals the critical VKH celerity exactly at the state of marginal VKH stability. The discrete growth rates at marginal stability will then be the exact VKH growth if also  $\delta_t^d$  is purely imaginary, which is the case if  $\Delta t \rightarrow 0$ . Wave growth shown in Subfigure 5.9a for vanishing time steps is thus very close to the differential growth as the considered state is close to the marginally stable state. Spatial discretisation errors are manifested foremost in the real components of  $c$ , *i.e.*, the wave speeds, which are often deemed to be of secondary importance.

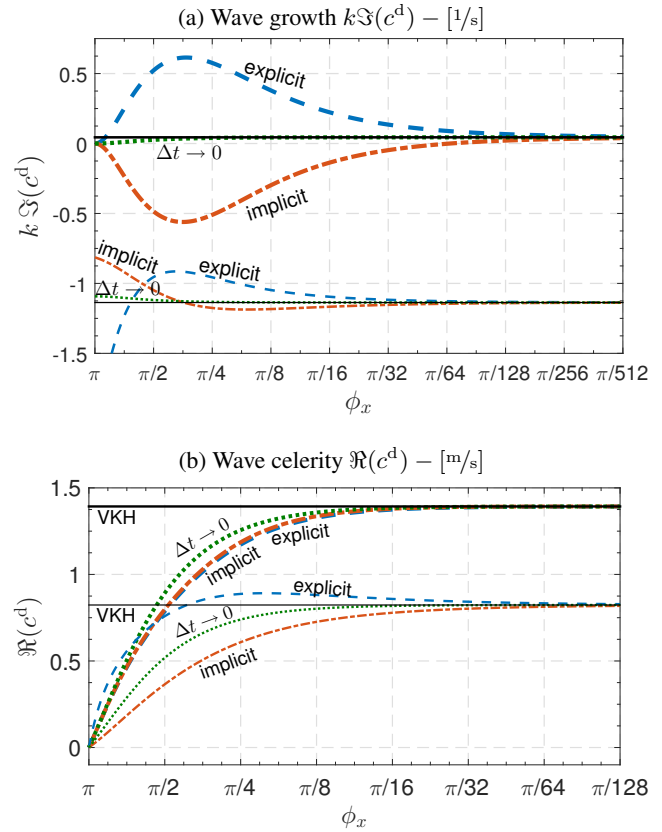


Figure 5.9: Non-staggered centred difference scheme with  $\nu = 0$ .

Figure 5.10 shows plots similar to the celerity plots shown back in Section 3, Figure 3.1, where viscous and inviscid Kelvin-Helmholtz celerities were compared under varying gas rates. The plots in Figure 5.10 show the errors from the time integration only, *i.e.*,  $\delta_t^d = \delta_t = -ikc$ , equivalent to the error as  $\Delta x$  approaches zero. A somewhat shorter wave, one diameter in length, has here been chosen to highlight the time integration effect, and the time step is  $\Delta t = 0.0025$  s.

The general trend of the time integration error is most easily observed from the thinner lines in Figure 5.10, showing the celerities in the inviscid case  $S \equiv 0$ . These lines would follow the abscissa if not for the error, as in Figure 3.1. The effect of the time integration error is to curve the celerity lines about the origin, convexly if the integration is foremost directed forwards in time (explicit,) and concavely if it is foremost directed backwards in time (implicit.) Errors are thus seen to increase with  $\Re(c^d)$ , which for the fast wave is means that it increases with decreasing  $Q_g/\mathcal{A}$ . Crank-Nicolson integration, abbreviated ‘C-N’ in the figure, is seen to be quite accurate in this case.

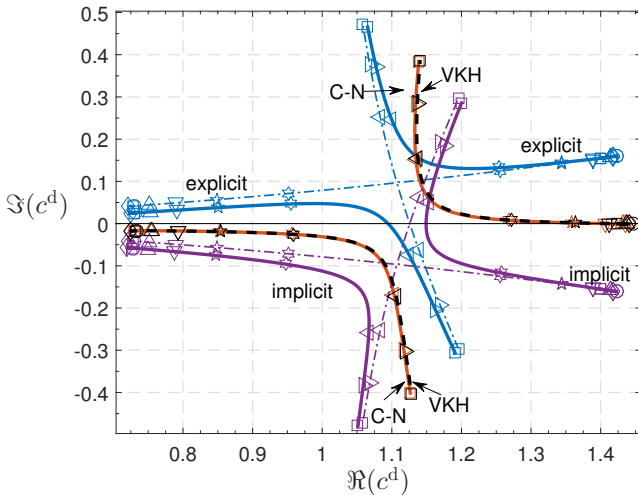


Figure 5.10: Complex celerity  $c$  under varying superficial gas velocity  $Q_g/\mathcal{A}$ , plotted with time integration error only ( $\delta_t^d = \delta_t$ .) Explicit, implicit and Crank-Nicolson time integrations are shown, cf. Table 1, along with the differential VKH celerity. Thinner lines (dot-dashed) show the corresponding explicit and implicit IKH celerities (where  $S \equiv 0$ .) The considered wave is one diameter long and  $\Delta t = 0.0025$  s. State parameters and markers for the superficial gas velocities are the same as in Figure 3.1

## 6 Concluding Remarks

Practically no computational effort is associated with the linear stability expressions. The examples presented in the previous section demonstrate some of the information instantaneously available through use of linear theory. This theory was shown to give quantitative discretization requirements for obtaining physical wave growth for any given wavelength. Conversely, it tells us what wavelength we can expect to see grow on any given grid, and how these waves move and grow in the discrete representation compared to in the differential model. Numerical errors were shown to manifest in both suppressed and excited growth, the latter being related to what is usually referred to as *numerical instabilities*. Some such instabilities were also observed in the low-wavenumber range where there is very little distinction be-

tween numerical and physical instabilities. Discrete stability theory was further able to demonstrate the way in which the time discretization affects predicted stability and to indicate appropriate values for the CFL number.

This information can aid in choosing reliable simulation parameters prior to simulation, and may give insight into whether or not simulation results can be considered physical.

## References

- A. H. Akselsen. Characteristic methods and Roe’s method for the incompressible two-fluid model for stratified pipe flow. Under review in the *International Journal of Multiphase Flow*, April 2016a.
- A. H. Akselsen. The stability of roll-waves in two-phase pipe flow. Submitted to the *International Journal of Multiphase Flow*, March 2016b.
- D. Barnea. Stability analysis of annular flow structure, using a discrete form of the ‘two-fluid model’. *International Journal of Multiphase Flow*, 17(6):705 – 16, 1991/11/. ISSN 0301-9322. URL [http://dx.doi.org/10.1016/0301-9322\(91\)90052-5](http://dx.doi.org/10.1016/0301-9322(91)90052-5).
- D. Barnea and Y. Taitel. Kelvin-Helmholtz stability criteria for stratified flow viscous versus non-viscous (inviscid) approaches. *International Journal of Multiphase Flow*, 19(4):639 – 649, 1993. ISSN 03019322. URL [http://dx.doi.org/10.1016/0301-9322\(93\)90092-9](http://dx.doi.org/10.1016/0301-9322(93)90092-9).
- Dvora Barnea and Yehuda Taitel. Non-linear interfacial instability of separated flow. *Chemical Engineering Science*, 49(14):2341 – 2349, 1994. ISSN 00092509. URL [http://dx.doi.org/10.1016/0009-2509\(94\)E0047-T](http://dx.doi.org/10.1016/0009-2509(94)E0047-T).
- D. Biberg. A mathematical model for two-phase stratified turbulent duct flow. *Multiphase Science and Technology*, 19(1):1 – 48, 2007. ISSN 0276-1459. URL <http://dx.doi.org/10.1615/MultSciTechn.v19.i1.10>.
- B.S. Brook, S.A.E.G. Falle, and T.J. Pedley. Numerical solutions for unsteady gravity-driven flows in collapsible tubes: evolution and roll-wave instability of a steady state. *Journal of Fluid Mechanics*, 396:223 – 56, 1999/10/10. ISSN 0022-1120. URL <http://dx.doi.org/10.1017/S0022112099006084>.
- J. H. Ferziger and M. Peric. *Computational Methods for Fluid Dynamics*. Springer, Berlin, 1999.
- William D. Fullmer, Victor H. Ransom, and Martin A. Lopez De Bertodano. Linear and nonlinear analysis of an unstable, but well-posed, one-dimensional two-fluid model for two-phase flow based on the inviscid Kelvin-Helmholtz instability. *Nuclear Engineering and Design*, 268:173 – 184, 2014. ISSN 00295493. URL <http://dx.doi.org/10.1016/j.nucengdes.2013.04.043>.
- D. Gidaspow. Multiphase flow and fluidization. *Journal of Fluid Mechanics*, 287:405 – 405, 1995. ISSN 00221120.
- H. Holmås. Numerical simulation of transient roll-waves in two-phase pipe flow. *Chemical Engineering Science*, 65(5):1811 – 25, 2010. ISSN 0009-2509. URL <http://dx.doi.org/10.1016/j.ces.2009.11.031>.
- R.I. Issa and M.H.W. Kempf. Simulation of slug flow in horizontal and nearly horizontal pipes with the two-fluid model. *International Journal of Multiphase Flow*, 29(1):69 – 95, 2003. ISSN 0301-9322. URL [http://dx.doi.org/10.1016/S0301-9322\(02\)00127-1](http://dx.doi.org/10.1016/S0301-9322(02)00127-1).
- G.W. Johnson. *A Study of Stratified Gas-Liquid Pipe Flow*. PhD thesis, Univ. Oslo, 2005. dr. scient.

Jun Liao, Renwei Mei, and James F. Klausner. A study on the numerical stability of the two-fluid model near ill-posedness. *International Journal of Multiphase Flow*, 34(11):1067 – 1087, 2008. ISSN 03019322. URL <http://dx.doi.org/10.1016/j.ijmultiphaseflow.2008.02.010>.

Himanshu Pokharna, Michitsugu Mori, and Victor H. Ransom. Regularization of two-phase flow models. *J. Comput. Phys.*, 134(2):282–295, July 1997. ISSN 0021-9991. doi: 10.1006/jcph.1997.5695. URL <http://dx.doi.org/10.1006/jcph.1997.5695>.

H.B. Stewart. Stability of two-phase flow calculation using two-fluid models. *Journal of Computational Physics*, 33(2):259 – 70, 1979. ISSN 0021-9991. URL [http://dx.doi.org/10.1016/0021-9991\(79\)90020-2](http://dx.doi.org/10.1016/0021-9991(79)90020-2).

Y. Taitel and A.E. Dukler. A model for predicting flow regime transitions in horizontal and near horizontal gas-liquid flow. *AIChE Journal*, 22(1): 47 – 55, 1976/01/. ISSN 0001-1541. URL <http://dx.doi.org/10.1002/aic.690220105>.

J. VonNeumann and R. D. Richtmyer. A method for the numerical calculation of hydrodynamic shocks. *Journal of Applied Physics*, 21(3):232–237, 1950. doi: <http://dx.doi.org/10.1063/1.1699639>. URL <http://scitation.aip.org/content/aip/journal/jap/21/3/10.1063/1.1699639>.

## A A Roe Scheme

The Roe scheme is commonly written

$$\frac{\mathbf{v}_j^{n+1} - \mathbf{v}_j^n}{\Delta t} + \frac{\mathbf{f}_{j+\frac{1}{2}} - \mathbf{f}_{j-\frac{1}{2}}}{\Delta x} = \mathbf{s}_j$$

where  $\mathbf{f}_{j\pm\frac{1}{2}}$  are the fluxes in the solution of the linearized Riemann problem

$$\mathbf{v}_t + \left( \frac{\partial \mathbf{F}}{\partial \mathbf{V}} \right)_{j+\frac{1}{2}}^{\text{Roe}} \mathbf{v}_x = 0 \quad (\text{A.1})$$

$$\mathbf{v}(x, 0) = \mathbf{v}_j, (x < 0); \quad \mathbf{v}(x, 0) = \mathbf{v}_{j+1}, (x > 0)$$

at each cell face  $x_{j+\frac{1}{2}}$ .  $\frac{\partial \mathbf{F}}{\partial \mathbf{V}}_{j+\frac{1}{2}}^{\text{Roe}}$  is the Roe-average of the Jacobian (2.5), constant in each Riemann problem. Using arithmetic mean notation  $\bar{w} = \frac{1}{2}(w_j + w_{j+1})$ , the Roe matrix of model (2.3) is

$$\frac{\partial \mathbf{F}}{\partial \mathbf{V}}_{j+\frac{1}{2}}^{\text{Roe}} = \frac{\partial \mathbf{f}}{\partial \mathbf{v}} \Big|_{\bar{\mathbf{w}}, \tilde{\mathcal{H}}'}$$

the Jacobian evaluated with the mean primitive variables

$$\bar{\mathbf{w}} = (\bar{a}_\ell, \bar{a}_g, \bar{u}_\ell, \bar{u}_g)^T$$

and

$$\tilde{\mathcal{H}}' = \begin{cases} \frac{h_{j+1} - h_j}{a_{\ell,j+1} - a_{\ell,j}}, & a_{\ell,j+1} \neq a_{\ell,j} \\ \mathcal{H}'(\bar{a}_\ell), & \text{otherwise} \end{cases}$$

replacing  $\mathcal{H}'$ .

The flux solution of (A.1) may be written

$$\mathbf{f}_{j+\frac{1}{2}} = \bar{\mathbf{f}} - \frac{1}{2} \mathbb{L}^{-1} |\Lambda| \mathbb{L} (\mathbf{v}_{j+1} - \mathbf{v}_j) \quad (\text{A.2})$$

where

$$|\Lambda| = \begin{pmatrix} |\lambda^+| & 0 \\ 0 & |\lambda^-| \end{pmatrix}, \quad \text{and} \quad \mathbb{L} = \begin{pmatrix} 1 & 1/\varkappa \\ 1 & -1/\varkappa \end{pmatrix}$$

are the absolute eigenvalue and eigenvector matrices of  $\left( \frac{\partial \mathbf{F}}{\partial \mathbf{V}} \right)_{j+\frac{1}{2}}^{\text{Roe}}$ , respectively. These are evaluated from (2.6) and (2.7) at the mean state  $\bar{\mathbf{w}}$  with  $\tilde{\mathcal{H}}'$  replacing  $\mathcal{H}'$ .

## B Transformation Matrices

Conversion between primitive variables  $\mathbf{w} = (a_\ell, a_g, u_\ell, u_g)^T$  and conservative variables  $\mathbf{v} = (a_\ell, [\rho u]_\ell^T)$  of the *incompressible* system (obeying (2.4)) is often useful. Transformation matrices for these are

$$\frac{\partial \mathbf{V}}{\partial \mathbf{W}} = \begin{pmatrix} 1 & 0 & 0 & 0 \\ 0 & 0 & \rho_\ell & -\rho_g \end{pmatrix}, \quad (\text{B.1a})$$

$$\frac{\partial \mathbf{W}}{\partial \mathbf{V}} = \frac{1}{A_\ell A_g \rho^*} \begin{pmatrix} A_\ell A_g \rho^* & 0 \\ -A_\ell A_g \rho^* & 0 \\ \rho_g (U_g - U_\ell) & A_g \\ \rho_\ell (U_g - U_\ell) & -A_\ell \end{pmatrix}. \quad (\text{B.1b})$$